^{19}F NMR and defect spins in vacuum-annealed $LaO_{0.5}F_{0.5}BiS_2$

S. Yadav,[1,*] S. Delgado,[1,†] O. O. Bernal,[1,‡] D. E. MacLaughlin,[2] Y. Liu,[3] D. Jiang,[3] O. Santana,[3] Lei Shu,[4] K. Huang,[4,§] D. Yazici,[5,¶] and M. B. Maple[5]

[1]*Department of Physics and Astronomy, California State University, Los Angeles, California 90032, USA*
[2]*Department of Physics and Astronomy, University of California, Riverside, California 92521, USA*
[3]*Department of Chemistry and Biochemistry, California State University, Los Angeles, California 90032, USA*
[4]*State Key Laboratory of Surface Physics, Department of Physics, Fudan University, Shanghai 200433, China*
[5]*Department of Physics, University of California, San Diego, La Jolla, California 92093, USA*

(Received 16 August 2024; revised 20 November 2024; accepted 26 November 2024; published 13 December 2024)

We report results of magnetization and ^{19}F NMR measurements in the normal state of as-grown vacuum-annealed $LaO_{0.5}F_{0.5}BiS_2$. The magnetization is dominated by a temperature-independent diamagnetic component and a field- and temperature-dependent paramagnetic contribution $M_\mu(H,T)$ from a ∼1000 ppm concentration of local moments, an order of magnitude higher than can be accounted for by measured rare-earth impurity concentrations. $M_\mu(H,T)$ can be fit by the Brillouin function $B_J(x)$ or, perhaps more realistically, a two-level $\tanh(x)$ model for magnetic Bi $6p$ ions in defect crystal fields. Both fits require a phenomenological Curie-Weiss argument $x = \mu_{\rm eff}H/(T+T_W)$, $T_W \approx 1.7$ K. There is no evidence for magnetic order down to 2 K, and the origin of T_W is not clear. ^{19}F frequency shifts, linewidths, and spin-lattice relaxation rates are consistent with purely dipolar ^{19}F/defect-spin interactions. The defect-spin correlation time $\tau_c(T)$ obtained from ^{19}F spin-lattice relaxation rates obeys the Korringa relation $\tau_c T = \text{const}$, indicating the relaxation is dominated by conduction-band fluctuations.

DOI: 10.1103/PhysRevB.110.235132

I. INTRODUCTION

The discovery of layered BiS_2-based superconductors [1,2] opened a new venue of research in the field, adding considerably to the existing list of layered superconducting materials. In particular, the rare-earth-based compound series $LnO_{1-x}F_xBiS_2$, Ln = La, Ce, Pr, Nd, Sm, and Yb, has been studied extensively in the search for higher superconducting temperatures T_c; see, e.g., Refs. [3–5] and references therein. The highest T_c has been achieved for Ln = La, for which $T_c^{\rm max} \sim 11.5$ K for samples annealed under hydrostatic pressure (HP) [6]. $LaO_{1-x}F_xBiS_2$ (LOFBS) grown at ambient pressure reaches $T_c \sim 10.6$ K [6,7] under pressure, which is the next highest value of T_c in this series.

As-grown LOFBS powder samples ($T_c \sim 3$ K) show signs of local superconducting phases for temperatures as high as 10 K [6]. This should be suggestive, and in fact similar signs observed in tunneling spectra for $Bi_4O_4S_3$ [8] inspired the search for higher T_c in the BiS_2 compounds [6]. Replacement of La by other Ln ions is seen to induce stable bulk SC as the ion's size decreases, but with T_c's less than that for La [4]. Similarly, stabilizing bulk superconductivity by replacing S for Se does not yield any higher T_c; see Ref. [6] for details.

The reasons for the lack of coherence in the superconducting fluid have apparently not been elucidated. The importance of magnetism to superconducting behavior might also be expected by the prediction [9] and potential confirmation [10] of spatial spin textures induced by spin-orbit coupling via Rashba [11] and Dresselhaus [12] effects in other systems. There appears to be a consensus regarding the conventional nature of the superconductivity in LOFBS.

Very little has been reported on the magnetic properties of the normal state from which the superconducting phase develops [6,13,14]. Magnetic susceptibility measurements reported to date do not go to temperatures higher than ∼20 K or applied fields higher than those for which the effects of magnetism can be avoided or minimized. No NMR measurements have been reported on this compound.

This paper reports results of magnetization and ^{19}F NMR measurements in the normal state of as-grown vacuum-annealed LOFBS. The observed magnetization is diamagnetic and constant above 100 K, below which it exhibits Brillouin-function and Curie-Weiss–type field and temperature dependencies typical of local-moment paramagnetism. With a phenomenological Curie-Weiss form for the argument $x = \mu_{\rm eff}H_0/k_B(T+T_W)$, either a Brillouin function $B_J(x)$ or the two-level version $\tanh(x)$ provides a good fit to the data with fit values ∼1000 ppm for the local-moment

*Present address: New Mexico Institute of Mining and Technology, Socorro, NM 87801, USA.
†Present address: Division of Physics, Mathematics and Astronomy, Caltech, Pasadena, California 91125, USA.
‡Contact author: obernal@calstatela.edu
§Present address: Lawrence Livermore National Laboratory, Livermore, California 94550, USA.
¶Present address: Faculty of Applied Physics and Mathematics and Advanced Materials Centre, Gdańsk University of Technology, 80-233 Gdańsk, Poland.

 ©2024 American Physical Society

concentration. However, measurement of impurity levels by mass spectrometry reveals 150 ppm Ce, 31 ppm Gd, and traces of other $3d$ and $4f$ impurities. Thus, the dilute local-moment magnetization in LOFBS is intrinsic, most likely due to Bi $6p$ ions decoupled from the conduction band by defects.

This is reminiscent of relatively recent findings in studies of sp systems containing no d or f ions. Dilute magnetic moments of order $1\mu_B$ have been associated with defect-induced magnetism in graphite and graphene [15–20]. Noncarbon materials have also been found to house magnetic moments of order $1\mu_B$ to $4\mu_B$ induced by defects; these include wide-gap III nitrides (GaN and BN) [21] and the dielectric oxide system HfO_2 [22,23]. Disordered ZnO and TiO_2 are also magnetic [24,25].

Pertinent to this study, Bi-containing materials have also been found to display unexpected magnetism [26–28]. These systems exhibit weak paramagnetism, and local fields of up to 250 G are observed at Bi sites using NQR, SQUID, and μSR techniques. A strong coupling between crystal electric field (CEF) and magnetic order is reported for Bi-based oxides in which a magnetoelectric effect linear in magnetic field is observed [28]. Reviews [25,29] give further information and references on this topic.

^{19}F NMR frequency shifts, linewidths, and spin-lattice relaxation rates have been measured. Spin echos [30] were used to determine the shift and line shape (the Fourier transform of the echo shape) due to the static field distribution at ^{19}F sites. The ^{19}F line in LOFBS is Voigtian, i.e., a convolution of Gaussian and Lorentzian distributions. The Lorentzian linewidth $1/T_{2e}^*(T)$ is expected from dipolar and/or Ruderman-Kittel-Kasuya-Yoshida (RKKY) coupling to dilute local moments [31]; our observation that the NMR frequency shift $K(T)$ and $1/T_{2e}^*(T)$ both vary linearly with the intrinsic magnetization $M_\mu(T)$[1] is good evidence for this and their common origin.

The observed ^{19}F NMR spin-lattice relaxation function is a stretched exponential $\exp[-(t/\tau_1)^p]$, $p < 1$. This indicates a spatially inhomogeneous distribution of relaxation rates, as expected from a dilute local-moment scenario [32–34]. The relaxation rate $1/\tau_1(T)$ exhibits a nonmonotonic temperature dependence with a maximum in the neighborhood of 10 K, and is considerably suppressed by field. The power p is roughly constant (0.70–0.75) at low temperatures, increasing slightly above 100 K. The observed values of $1/T_{2e}^*$ and $1/\tau_1(T)$ are consistent with a dipolar ^{19}F/defect-spin coupling, and rule out a significant conduction-band-mediated RKKY interaction between defect spins and ^{19}F nuclei. The $1/\tau_1(T)$ data also place a low upper limit on any ^{19}F Korringa relaxation rate due to conduction-band spin fluctuations.

Thus, the ^{19}F relaxation is dominated by fluctuations of the defect spins. These exhibit a temperature-dependent correlation time $\tau_c(T)$ roughly of the Korringa form $\tau_c(T)T =$ const, indicating a dominant defect-spin/exchange coupling with conduction-band states. This would be inconsistent with extrinsic magnetic impurities replacing La^{3+} in the blocking layers of the crystal structure, as would be the case for Ce or Gd ions, because of the considerable distance (> 6 Å) between blocking and conduction layers. The results suggest instead a small but significant exchange interaction $\mathcal{J}_{ex} = 3.6$ meV between defect spins and conduction-layer band states, consistent with the defects being associated with BiS_2 planes.

Our measurements of magnetization and ^{19}F NMR in LOFBS lead us to conclude that the observed local-moment magnetism is due to a dilute distribution of crystal defects. This may be related to recent results [35] where bond disorder in the BiS_2 planes is described as potentially being a conduction-electron trap. Our results indicate that the magnetic defects interact principally with the BiS_2-plane conduction band rather than each other, but that $\mathcal{J}_{ex}$ is far too weak to have a significant effect on the superconducting state.

The paper is organized as follows. Section II gives brief descriptions of sample preparation and experimental techniques. Results of magnetization and ^{19}F NMR line shape, linewidth, frequency shift, and spin-lattice relaxation measurements are reported in Sec. III and discussed in Sec. IV. A summary and conclusions follow in Sec. V.

II. EXPERIMENT

A. Sample

Polycrystalline LOFBS was prepared by solid-state reaction at ambient pressure as described previously [36,37]. The sample was characterized by x-ray powder diffraction, electrical resistivity, magnetic susceptibility, and specific-heat measurements to determine its superconducting properties. The starting purity of the precursor powders of La_2O_3, LaF_3, La_2S_3, and Bi_2S_3 used in the preparation of the sample exceeded 99.9% in most cases [36].

Trace magnetic impurities in the sample were fully characterized. Preliminary analytical studies indicated Ce and Gd as dominant impurities in the starting material. A Perkin-Elmer ELAN 9000 inductively coupled plasma mass spectrometer (ICP-MS) was used to determine impurity concentrations. Initial measurements without reference standards yielded Ce and Gd concentrations of ∼90 and ∼17 ppm, respectively, with Sm about the same as Gd, Tb, and Yb considerably lower ($\lesssim 5$ ppm) and Nd, Dy, Ho, Tm, Co, Cr, Fe, and Ni all $\lesssim 1$ ppm.

With reference standards the accuracy of an ICP-MS measurement is improved considerably. Ce and Gd standard solutions with concentrations 1–200 ppb were prepared from commercial ICP-MS standards (1000 ppm) through serial dilution using using 2% nitric acid. The standard solutions were then used to create calibration curves for Ce and Gd. To prepare the LOFBS ICP-MS samples, 29.68 mg of material was first fully digested in 5 mL nitric acid in a heated sonicator. The digested sample solution was then diluted to 250 mL in a volumetric flask using 2% nitric acid. Three pieces were measured from different parts of the sample for consistency. The results were 150(3) ppm Ce and 31(1) ppm Gd, where the uncertainties are the variations between the pieces.

The unit cell of LOFBS is shown in Fig. 1. Conduction-band states and superconductivity are considered to be restricted to the Bi-S bilayers; the blocking La-O/F bilayers are insulating.

[1]Or, equivalently, with the intrinsic susceptibility $\chi_\mu(T) = M_\mu(T)/H_0$.

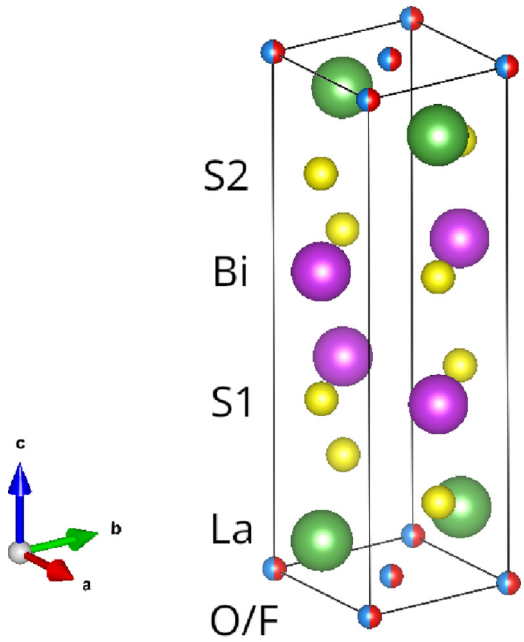


FIG. 1. Unit cell of LOFBS.

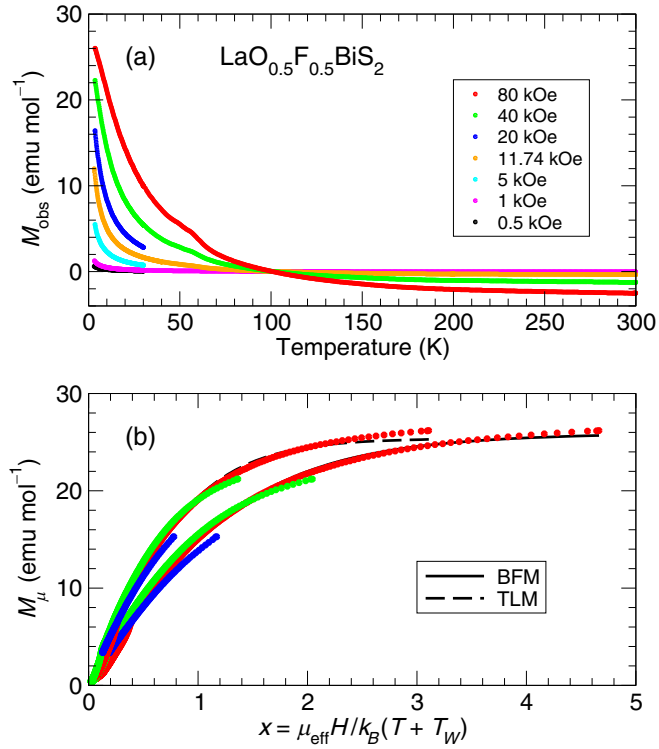


FIG. 2. (a) Temperature dependence of observed magnetization $M_{obs}(H, T)$ in LOFBS powder. (b) Fits of the Brillouin function $B_J(x)$ (solid curve) and $\tanh(x)$ (dashed curve), $x = \mu_{eff}H/k_B(T + T_W)$, to the intrinsic magnetization $M_\mu(H, T)$. See text and Sec. IV A 2 for details.

Superconducting properties of the sample have been reported previously [3–5,36–38]. The zero-field superconducting transition occurs between 2.8 and 2.9 K. In a field 0f 10 kOe there is a slight reduction of the resistivity below 3 K but no bulk transition above 2 K [38].

B. Magnetization

The sample magnetization was measured using a Quantum Design PPMS system configured with a vibrating sample magnetometer. Measurements were made for temperatures between 3 and 300 K and magnetic fields in the range 0.5–80 kOe.

C. NMR

^{19}F is a spin-$\frac{1}{2}$ nucleus with a large magnetic moment ($2.63\mu_N$). It is not affected by electric field gradients, and the resonance line in LOFBS is narrow (Sec. III B). ^{19}F NMR experiments were carried out using a standard pulsed NMR spectrometer with phase-sensitive detection over the temperature range 3–300 K for applied fields of 11.741, 20, and 40 kOe. ^{19}F spin echoes were produced using the Hahn $\pi/2$-π pulse sequence [30].

a. Frequency shifts. ^{19}F frequency shifts were measured in an applied field $H_0 = 11.741$ kOe for temperatures between 1.8 and 300 K. The ^{19}F frequency in CaF_2 [39–41] was used as a reference; samples of both LOFBS and CaF_2 were included in the NMR coil [41]. A careful characterization of the CaF_2 line was carried out to confirm it provided a consistent reference over the full range of temperatures. This line is nearly a rectangle in the frequency domain [39], so that the time-domain signals exhibit Lowe-Norberg beats [40]. To facilitate the fits the CaF_2 line shape was approximated by a power exponential function $f(\nu) = \exp\{-[(\nu-\nu_0)/\Delta\nu)^q\}$ with $q \approx 5$ from the fits; this shape is independent of temperature. Fits to the combined spectra are described below in Sec. III B 1.

b. Line shapes, linewidths. The line shapes and linewidths of the NMR spectra were determined in the time domain from the relaxation rates of the echo-decay signals (Sec. III B 2). The signals were fit to a Voigtian function, which is the product of a Gaussian $\exp[1/2(t/T_{2G}^*)^2]$ and a Lorentzian $\exp(t/T_{2e}^*)$ in the time domain. The relaxation rates $1/T_{2G}^*$ and $1/T_{2e}^*$ are the linewidths of the corresponding components of the Voigtian. In LOFBS these are considerably faster than the dynamic spin-lattice relaxation rates (Sec. III C), and are therefore attributed to broadening by inhomogeneous distributions of static local fields.

c. Spin-lattice relaxation. The narrow line allowed complete inversion of the ^{19}F magnetization by a single rf pulse. The recovery signal $S(t)$ after this pulse is related to the normalized relaxation function $s(t)$ [$s(0) = 1$, $s(\infty) = 0$] by

$$S(t) = S_f + (S_i - S_f)s(t), \tag{1}$$

where S_i and S_f are the initial and final recovery signals, respectively. Results are discussed below in Sec. III C.

III. RESULTS

A. Magnetization

Figure 2(a) shows the observed magnetization $M_{obs}(H, T)$ in LOFBS. The sample is diamagnetic above ~100 K, and exhibits the Curie-Weiss–type behavior typical of local-moment

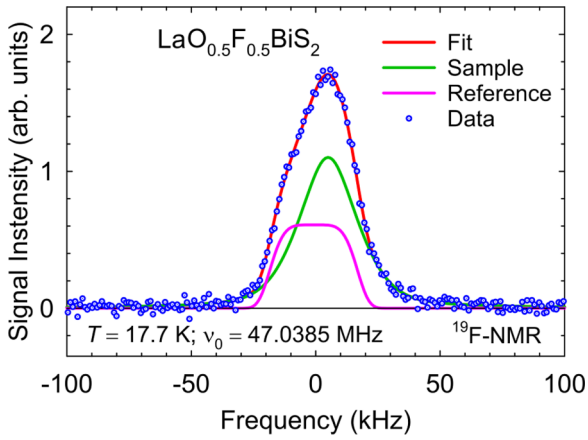


FIG. 3. Fit of a two-component line to a ^{19}F spectrum from a sample containing both LOFBS powder and a CaF_2 reference.

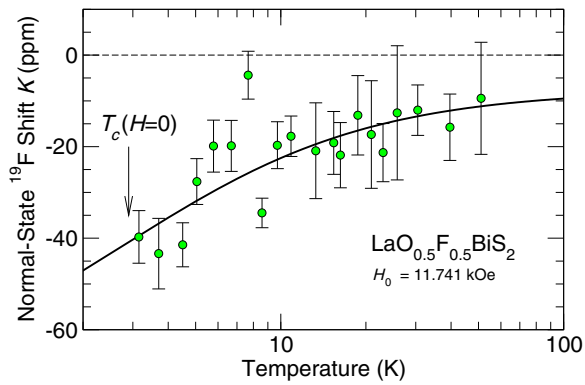


FIG. 4. Normal-state temperature dependence of ^{19}F frequency shift in LOFBS powder with respect to a $CFCl_3$ reference. Arrow: zero-field superconducting transition temperature $T_c(H{=}0)$. Curve: $K(T)$ from a linear Clogston-Jaccarino fit to normal-state K-χ_μ data (Fig. 10).

paramagnetism. The temperature-dependent paramagnetism $M_\mu(H,T)$ was obtained by subtraction of a temperature-independent diamagnetic term $M_0(H)$ and small contributions from the trace Ce and Gd impurities (Sec. II A above).

Two local-moment models have been fit to the $M_\mu(H,T)$ data, as shown in Fig. 2(b). The *Brillouin function model* (BFM, solid curve) uses a modified Brillouin function [42]

$$M_\mu(H,T) = N_0 c \mu_{\rm eff} B_J(x),$$
$$x = \frac{\mu_{\rm eff} H}{k_B(T+T_W)} \quad \text{(BFM)}, \tag{2}$$

where N_0 is the formula-unit density, c is the concentration of local moments, and $\mu_{\rm eff}$ is the effective local magnetic moment. The Weiss temperature T_W is included phenomenologically because of the observed Curie-Weiss behavior of the low-field susceptibility. As discussed in Sec. IV A 2, this is not a good approximation at high fields, which is likely to account for the deviations for large x.

The *two-level model* (TLM, dashed curve) uses a hyperbolic tangent function

$$M_\mu(H,T) = cN_0\mu_{\rm eff}\tanh(x) \quad \text{(TLM)}, \tag{3}$$

with x as in Eq. (2). This is the BFM with J fixed at $\frac{1}{2}$, but the interpretation of the effective moment that results from the model differs in the two models as discussed below in Sec. IV A 2.

The fits and resulting parameter values are discussed in Sec. IV A 2. M_μ is consistent with $\gtrsim$1100 ppm of local moments, an order of magnitude or more larger than the measured trace Gd and Ce levels. The large-x deviations are smaller for the BFM than for the TLM, but this cannot be taken as evidence for the former because of the inapplicability of the Curie-Weiss approximation noted above.

B. ^{19}F spectra

1. ^{19}F *frequency shifts*

Frequency shifts were obtained from Fourier transforms of spin echoes from samples containing both LOFBS and CaF_2. An example of the fit of an observed spectrum to the sum of these contributions is shown in Fig. 3.

The center of the LOFBS line with respect to that of CaF_2 could be determined by fitting the combined spectra to a sum of two functions: a modified Gaussian for CaF_2 (Sec. II C 0 a) and a symmetric function for LOFBS. For the latter Gaussian and Lorentzian fits yield the same line centers to within statistical errors, but a pseudo-Voigtian [43] superposition of Gaussian and Lorentzian terms accounts for the spectral tails better and reduces the systematic uncertainty of the shift.

Figure 4 gives the normal-state ($T > T_c = 2.9$ K [37]) temperature dependence of the frequency shift K with respect to $CFCl_3$, a reference material for which the field at the ^{19}F site is close to the vacuum value [44]. The CaF_2 chemical shift of $-108.0(2)$ ppm with respect to $CFCl_3$ [44] was used to correct the observed shift. $|K(T)|$ decreases with increasing temperature, reminiscent of $1/T_{2e}^*(T)$ (Fig. 6 below). The curve in Fig. 4 is $K(T)$ from the fit of the linear Clogston-Jaccarino [45] relation $K(T) = K_0 + A_K\chi_\mu(T)$, where χ_μ is the defect susceptibility.

2. *Spin-echo shapes, linewidths*

The echo relaxation is purely static (cf. Sec. III C). It is expected to have two contributions from the local field distribution: a Gaussian distribution from nuclear dipolar fields [30], and a Lorentzian distribution from dilute defect dipolar fields [31]. Thus, a Voigtian (convolution of Gaussian and Lorentzian) distribution is expected in the frequency domain, so that in the time domain the two components are simply a product.

For the ^{19}F echo and spin-lattice relaxation measurements a sample containing only LOFBS (no CaF_2) was prepared. Figure 5 shows typical in-phase and quadrature spin-echo signals. The two quadrature signals are the Voigtian functions

$$S_{ip}(t) = \exp\left\{-|t-t_0|/T_{2e}^* - \tfrac{1}{2}[(t-t_0)/T_{2G}^*]^2\right\} \times \cos[\delta\omega(t-t_0)] \tag{4}$$

and

$$S_q(t) = \exp\left\{-|t-t_0|/T_{2e}^* - \tfrac{1}{2}[(t-t_0)/T_{2G}^*]^2\right\} \times \sin[\delta\omega(t-t_0)], \tag{5}$$

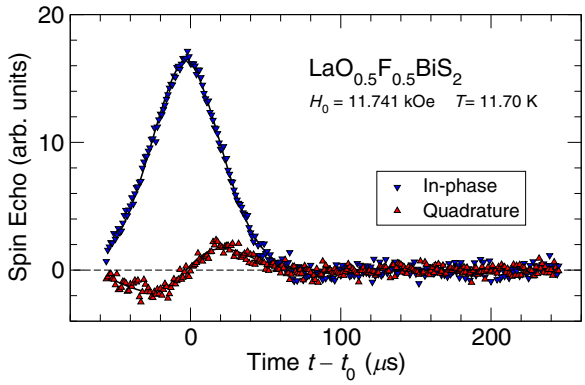


FIG. 5. Representative ^{19}F in-phase and quadrature spin-echo signals in LOFBS powder. Curves: fits of Eqs. (4) and (5) to the data.

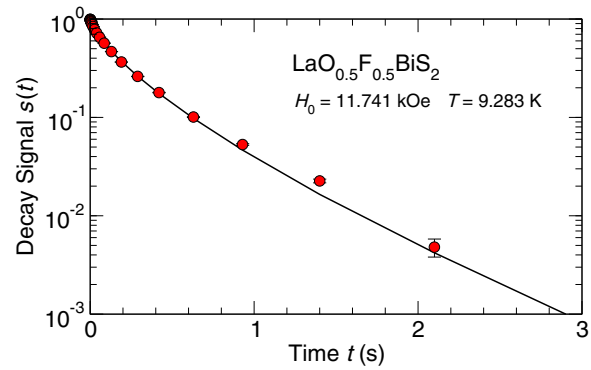


FIG. 7. Semilogarithmic plot of observed ^{19}F spin-lattice relaxation function $s(t)$ in LOFBS powder, showing upward curvature characteristic of inhomogeneously distributed relaxation.

which were fit to the in-phase and quadrature echo signals, respectively. Here t_0 is the refocusing time of the echoes, and the cosine and sine factors account for any difference $\delta\omega$ between the spectrometer and ^{19}F frequencies.

Phase-sensitive detection and simultaneous fit of both signals is essential: the Gaussian and cosine factors in $S_{ip}(t)$ are the same to second order and are therefore strongly correlated statistically, so that T_{2G}^* and $\delta\omega$ cannot be determined separately from a fit of Eq. (4) alone.

Figure 6 gives the temperature dependencies of $1/T_{2e}^*$ and $1/T_{2G}^*$. Gaussian relaxation is dominant, with a nearly temperature-independent rate of roughly 40 ms^{-1} $\approx$ 1.6 Oe in field units. Dipolar coupling to nearby ^{19}F and ^{139}La nuclei [46] yields a Gaussian width of $\sim$1.1 Oe, in reasonable agreement.

The exponential rate $1/T_{2e}^*$ is too small to be measured accurately above $\sim$30 K, and increases at lower temperatures. A Lorentzian contribution to the static field distribution proportional to the magnetization is expected from a dilute concentration of paramagnetic local moments [31].

C. ^{19}F spin-lattice relaxation

Figure 7 shows an example of an observed spin-lattice relaxation function $s(t)$ [Eq. (1)] from LOFBS. The upward curvature on the semilogarithmic plot indicates an inhomogeneous distribution of relaxation rates [32–34]. It is often modeled by a stretched exponential [34]

$$s(t) = \exp[-(t/\tau_1)^p], \quad p < 1 \tag{6}$$

motivated primarily by the result for direct host spin-lattice relaxation (no nuclear spin diffusion) by dilute paramagnetic local moments with a $1/r^3$ interaction. In a three-dimensional host $p = \frac{1}{2}$ [32,33,47]; in a two-dimensional host $p = 1/3$.[2]

Stretched-exponential fits to the data are discussed in Appendix A. Values of $1/\tau_1$ and p for fits using Eq. (6) are shown in Fig. 8.

For each field $1/\tau_1(T)$ is strongly nonmonotonic, with a maximum in the neighborhood of 10 K. The rate is considerably suppressed by field. The power p is roughly constant at 0.70–0.75 at low temperatures, increasing to $\sim$0.85 above 100 K. It exhibits little if any field dependence.

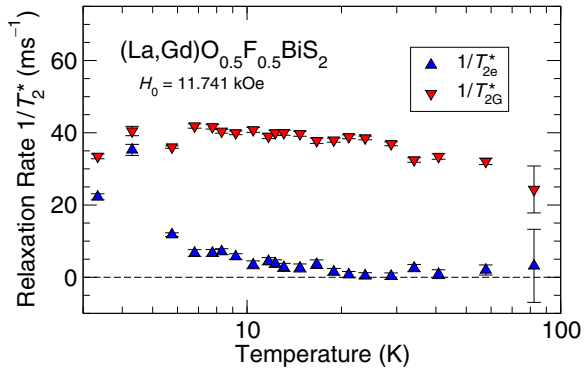


FIG. 6. Temperature dependence of ^{19}F relaxation rates $1/T_2^*$ in LOFBS powder from fits of Eqs. (4) and (5) to spin-echo data. $1/T_{2e}^*$: exponential rate. $1/T_{2G}^*$: Gaussian rate.

IV. DISCUSSION

A. Magnetization

1. *Temperature-independent magnetization*

The temperature-independent susceptibility $\chi_0 = M_0(H)/H$ of LOFBS was obtained from plots of $M_{\rm obs}(H,T)$ vs $1/T$ by extrapolating to $1/T = 0$. $\chi_0 = \chi_{\rm core}^{\rm dia} + \chi_P + \chi_L + \chi_{\rm orb}$, where $\chi_{\rm core}^{\rm dia}$ is the core diamagnetic susceptibility [48,49], and χ_P, χ_L, and $\chi_{\rm orb}$ are the Pauli (paramagnetic), Landau (diamagnetic), and orbital contributions, respectively.

χ_P was estimated from reported Sommerfeld specific-heat coefficients $\gamma_{\rm spht} = C_{\rm el}(T)/T$ [36,50,51] using the free-electron relation $\chi_P = 3(\mu_B/\pi k_B)^2\gamma_{\rm spht}$. This includes correlation effects but does not take exchange enhancement into account [49]. The Landau and Pauli susceptibilities are related: $\chi_L = -\frac{1}{3}\chi_P(m/m^*)^2$ [42], where m is the electron mass and m^* is the effective mass including correlation effects. Estimates of m/m^* have been obtained [52] from the ratios of the above χ_P estimates to the average 0.424×10^{-4} emu/mol

[2]Unpublished: the calculation of Ref. [32] for three dimensions is easily modified for two dimensions.

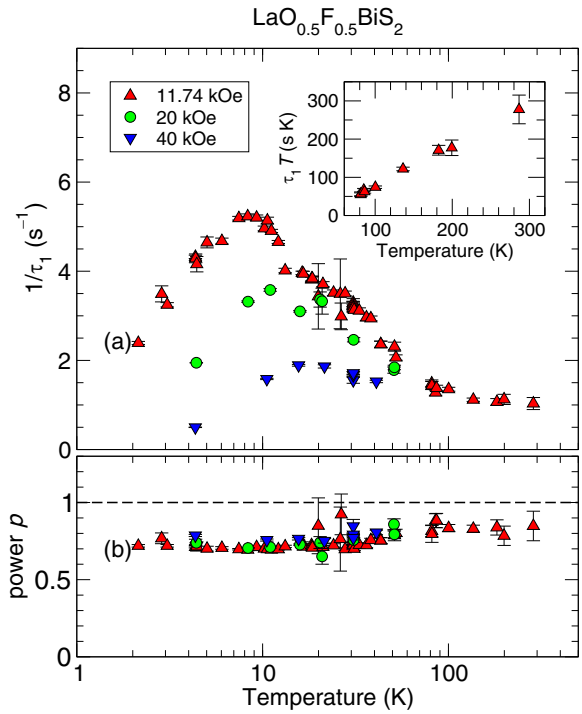


FIG. 8. ^{19}F stretched-exponential relaxation in LOFBS powder. (a) Stretched-exponential rate $1/\tau_1(T,H)$ [Eq. (6)]. Inset: $\tau_1(T)T$, $H_0 = 11.74$ kOe, at high temperatures. (b) Stretching power $p(T,H)$.

of two band-theoretical values without correlation [53,54]. Then $\chi_{\rm orb} = \chi_0 - \chi_{\rm core}^{\rm dia} - \chi_P - \chi_L$.

The results are given in Table I. The considerable variations in values of χ_P and related quantities are due to the variation in reported values of $\gamma_{\rm spht}$.

2. *Temperature-dependent magnetization; models*

For each field $M_0(H)$ and corrections for the trace Ce and Gd impurities were subtracted from $M_{\rm obs}(H,T)$ to obtain the intrinsic magnetization $M_\mu(H,T)$ [Fig. 2(b)]. The parameter values resulting from the fits of the BFM and TLM to $M_\mu(H,T)$ are given in Table II.

The two models are discussed below.

a. BFM. The Brillouin function describes the paramagnetism of ions with unfilled shells for which the ground-state

TABLE I. Temperature-independent magnetic susceptibility of LOFBS from high-temperature magnetization, estimated core diamagnetic ($\chi_{\rm core}^{\rm dia}$), Pauli ($\chi_P$), Landau diamagnetic ($\chi_L$), and orbital ($\chi_{\rm orb}$) contributions, and effective mass ratios m^*/m. Susceptibility units are 10^{-4} emu/mol. See text for details.

χ_0	$\chi_{\rm core}^{\rm dia}$	χ_P	m^*/m	χ_L	$\chi_{\rm orb}$
−0.461	−1.942[a]	0.347[b]	0.82	−0.172	1.306
”	”	0.270[c]	0.64	−0.221	1.432
”	”	0.453[d]	1.36	−0.104	1.010

[a]From Refs. [48] and [49].
[b]$\gamma_{\rm spht}$ from Ref. [36].
[c]$\gamma_{\rm spht}$ from Ref. [50].
[d]$\gamma_{\rm spht}$ from Ref. [51].

TABLE II. Parameters from fits of the BFM and TLM [Eqs. (2) and (3), respectively] to intrinsic magnetization $M_\mu(H,T)$ (Fig. 2).

Model	BFM	TLM
Concentration c (ppm)	1033(164)	1500(20)
Max. magnetization $M_{\rm sat}$ (emu/mol)	26.0(4)	25.4(2)
Effective moment $\mu_{\rm eff}$ (μ_B)	4.5(7)	3.03(3)
J	1.0(4)	1.52(2)[a]
Spin-orbit/CEF ratio λ/Δ (TLM)		−0.51(2)
g	4.4(1.7)[b]	2[c]
Weiss temperature T_W (K)	1.67(11)	1.73(10)

[a]$J = \mu_{\rm eff}/g$.
[b]$g = \mu_{\rm eff}/J$.
[c]Fixed (cf. Ref. [55]).

configuration is the lowest-lying $2J+1$ multiplet. A fit with the BFM [Eq. (2)] was made with g factor $g = \mu_{\rm eff}/J$, since the three parameters cannot all be left free. The resultant g value seems large. There is no evidence for magnetic order down to 2 K, and the origin of T_W is not clear.

A BFM fit using fixed Gd^{3+} ionic parameters $g = 2$, $J = S = \frac{7}{2}$, $\mu_{\rm eff} = 7$ yields a concentration ∼850 ppm, ∼30 times larger than the measured level of Gd impurities (Sec. II A). The trace Ce in the sample also cannot account for $M_\mu(H,T)$. No other d or f elements are present, so that one is led to suspect the presence of local-moment defects associated with Bi $6p$ states.

b. TLM. The TLM [Eq. (3)] is based on the conjecture that the sources of local magnetic moments are Bi $6p$ ions in crystal defects, e.g., bond disorder as in Ref. [35]. The energy levels of these electrons can be modeled as resulting from spin-orbit coupling combined with the CEF produced by a lack of inversion symmetry at the defect site [56].

Figure 9 is a schematic depiction of the TLM. It has two parameters, the spin-orbit coupling λ and the CEF splitting Δ between the $6p_x$ and $6p_y$ levels of the affected Bi atoms [55]. The lowest-lying of the three resulting levels is fully occupied by two of the three $6p$ electrons. The other two levels are higher and differ in energy by Δ, and the lower of these is half-filled by the remaining electron. Spin-orbit coupling changes this level's energy in first order by an amount proportional to

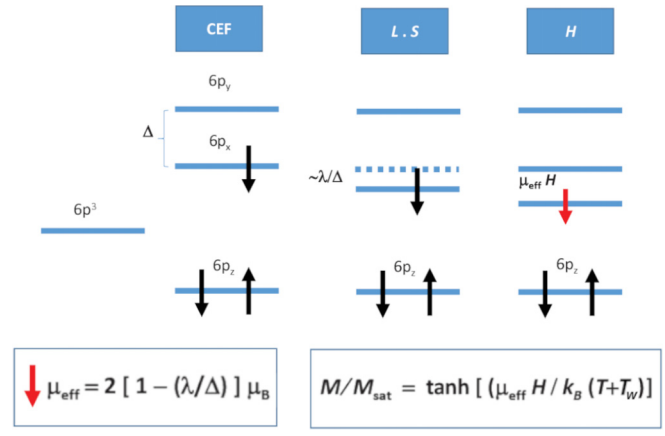


FIG. 9. Conjectured level scheme for the TLM.

λ/Δ, as depicted in Fig. 9. The level splits in a magnetic field by an amount proportional to the effective moment, which to first order is $\mu_{\rm eff} = g[1 - \lambda/\Delta]$ [55].

Of the two models, the TLM seems a more realistic description of Bi $6p$ magnetism, and the BFM-fit g value of 4.4 is hard to reconcile with Bi defect moments. Analysis of ^{19}F spin-lattice relaxation data using the TLM is given below in (Sec. IV C), but the results do not depend strongly on which model is used.

c. Curie-Weiss ansatz. The Curie-Weiss phenomenology used in the BFM and TLM fits is only valid for small argument x, and it is not surprising that there are systematic deviations for large x. If spin-spin interactions are involved the simplest scenario for taking them into account is the molecular-field approach, where interactions between spins are approximated by a single local field proportional to the system magnetization. The total field is then $H_0 + \Lambda M_\mu$, where Λ is the Weiss molecular field constant. The argument x of the BFM and TLM then becomes $x = \mu_{\rm eff}(H_0 + \Lambda M_\mu)/k_B T$.

Fits using this *ansatz* are shown in Appendix B. Agreement is not improved for large x and, more importantly, the maximum molecular field $\Lambda M_{\rm sat}$ is nearly 10 kOe. As discussed in Secs. IV B and IV C 3 below, ^{19}F NMR results indicate that this is four orders of magnitude larger than either dipolar or RKKY coupling fields. Curie-Weiss behavior can be due to CEF effects rather than spin-spin interactions [57], but a method of extending the Curie-Weiss phenomenology to large x has not yet been found.

B. ^{19}F spectra

1. ^{19}F *frequency shifts*

The Knight shift resulting from conduction-band paramagnetism is the largest term in simple metals, and is typically in the 10^3–10^4 ppm range. The small shifts in LOFBS ($\lesssim 100$ ppm, Fig. 4) suggest a low conduction-band density at the ^{19}F site [53,54], consistent with the conduction channel being localized on the BiS_2 layers (Fig. 1).

In addition, the normal-state temperature dependence of the shift indicates coupling between ^{19}F spins and a temperature-dependent contribution to the magnetism. An obvious candidate for this is the defect magnetism described above in Sec. III A.

Figure 10 is a Clogston-Jaccarino plot [45] of $K(T)$ data (Fig. 4) vs $\chi_\mu(T)$ for $T > T_c$. The linear fit yields intercept $K_0 = -7(3)$ ppm and slope $A_K = dK/d\chi_\mu = -0.033(6)$ mol/emu $= 184(3)$ G/μ_B. K_0 is the temperature-independent sum of the conduction-band Knight shift and a contribution from core diamagnetism [49]. These cannot be determined separately without further information.

The absolute field shift $\Delta H = H_0 K$ vs magnetization M_μ is linear with slope $A_{\Delta H} = d\Delta H/dM_\mu = A_K$ as defined above. Thus, the slope $A_{\Delta\omega} = d\Delta\omega/dM_\mu$ of the absolute frequency shift $\Delta\omega$ vs M_μ is also linear with slope $A_{\Delta\omega} = \gamma_n A_{\Delta H}$, where γ_n is the nuclear gyromagnetic ratio. $A_{\Delta\omega} = -0.83(15)$ ms^{-1}/emu/mol, and is compared with ^{19}F linewidth results in Sec. IV B 2 below.

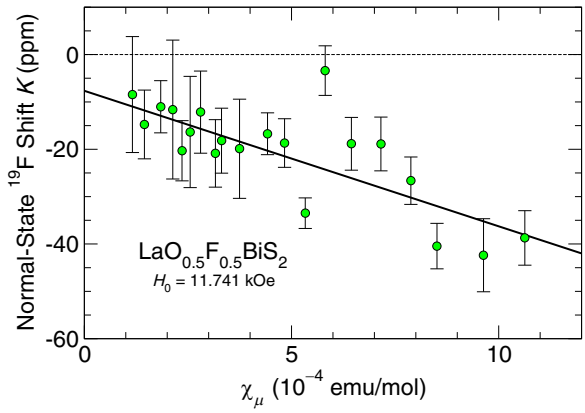


FIG. 10. Normal-state ^{19}F frequency shift $K(T)$ vs defect susceptibility $\chi_\mu(T)$ (Clogston-Jaccarino plot) in LOFBS powder, $T > T_c$. Line: linear fit to the data.

2. ^{19}F *linewidths*

The nearly temperature-independent Gaussian linewidth $1/T_{2G}^*$ is due to nuclear dipole-dipole interactions, whereas the Lorentzian linewidth (exponential rate) $1/T_{2e}^*$ arises from defect moments. There are two potential contributions to the latter [31]: defect-moment dipolar fields, and indirect RKKY interactions via conduction-electron polarization.

The dipolar contribution in a free-electron metal is given by

$$1/T_{2e}^{*\,\rm dip} = \frac{8\pi^2}{9\sqrt{3}} N_0 c\, \gamma_m \gamma_n \hbar \langle J_z \rangle \tag{7}$$

$$= A_{T_{2e}}^{\rm dip} M_\mu, \quad A_{T_{2e}}^{\rm dip} = \frac{8\pi^2 \gamma_n}{9\sqrt{3} V_{\rm mol}}, \tag{8}$$

where N_0 is the formula-unit density, c is the defect concentration, γ_m is the defect-spin gyromagnetic ratio, $\langle J_z \rangle$ is the defect polarization, M_μ is the molar defect magnetization, and $V_{\rm mol} = 68.05$ cm^3/mol is the molar volume.

The RKKY contribution is given by

$$1/T_{2e}^{*\,\rm RKKY} = \frac{4\pi}{3} A_{T_{2e}}^{\rm RKKY} \langle S_z \rangle, \text{ where} \tag{9}$$

$$A_{T_{2e}}^{\rm RKKY} = \frac{2\pi H_{\rm hf} N^2(E_F) \mathcal{J}_{\rm ex} E_F}{(2k_F)^3}; \tag{10}$$

here $H_{\rm hf}$ is the ^{19}F/conduction-band hyperfine coupling, $N(E_F)$ is the conduction-band density of states at the Fermi energy E_F, $\mathcal{J}_{\rm ex}$ is the defect-moment and conduction-band exchange interaction, and k_F is the Fermi wave vector.

In Sec. IV C $N(E_F)\mathcal{J}_{\rm ex}$ and an upper limit on $H_{\rm hf}$ are estimated from ^{19}F spin-lattice relaxation data. The resulting upper limit on $1/T_{2e}^{*\,\rm RKKY}$ ($\langle S_z \rangle = S$) is $9.3(3) \times 10^{-3}$ ms^{-1}, which is three orders of magnitude smaller than experimental values (Fig. 6). This is evidence that the dipolar interaction is dominant in LOFBS, which is assumed in the following.

Figure 11 is a Clogston-Jaccarino plot of $1/T_{2e}^*$ vs M_μ. $1/T_{2e}$ is linear in M_μ, with slope $A_{T_{2e}}^{\rm obs} = 2.8(2)$ ms^{-1}/(emu/mol). This is in reasonable agreement with the calculated dipolar value $A_{T_{2e}^*}^{\rm calc} = 1.94$ ms^{-1}/(emu/mol) [Eq. (8)], and is further evidence that the defect/^{19}F coupling

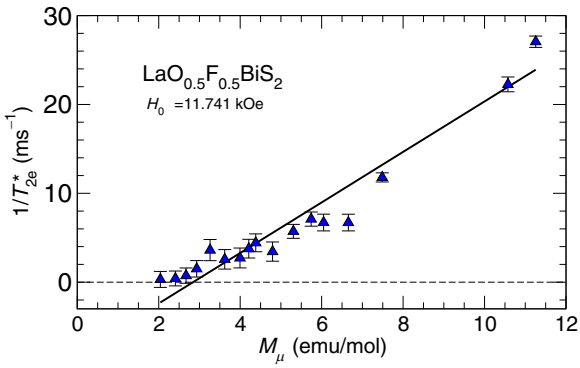


FIG. 11. Exponential echo relaxation rate $1/T_{2e}^*$ vs defect magnetization M_μ in LOFBS powder. Line: linear fit to the data.

is predominantly dipolar [31]. Dipolar coupling is also consistent with the observed spin-lattice relaxation in LOFBS, as discussed below in Sec. IV C 2. We note that $A_{T_{2e}^*}^{\rm obs}$ is somewhat larger than but comparable to $|A_{\Delta\omega}|$ (Sec. IV B 1).

The offset and corresponding negative value of the fit-line intercept in Fig. 11 are not well understood. They may be artifacts of the strong statistical correlation between $1/T_{2e}^*$ and $1/T_{2G}^*$ in fits of Eqs. (4) and (5) (correlation coefficient −0.894); this propagates systematic error between the parameters.

We conclude that $1/T_{2e}^*$ is the width of the Lorentzian defect dipole-field distribution in frequency units, and that $\Delta\omega$ is a rough estimate of its mean. We note that the mean dipolar shift vanishes for a randomly oriented powder sample with an isotropic susceptibility, but this is unlikely to be the case in LOFBS.

C. ^{19}F spin-lattice relaxation

1. Korringa relaxation?

From the inset to Fig. 8(a) there is no evidence for the Korringa spin-lattice relaxation $T_{1K}T = \text{const}$ expected from direct ^{19}F coupling to the conduction band or bands. The data suggest a rough lower limit on $T_{1K}T$ of ∼300 s K, but it is unlikely to be this small given the large high-temperature slope of $\tau_1 T$. Furthermore, Korringa relaxation is homogeneous and hence a simple exponential, but the power p of the observed stretched exponential shows no sign of approaching 1 at high temperature [Fig. 8(b)]. Introducing a simple exponential to the relaxation fit function worsens the least-squares fit [Fig. 13(b)].

For a free-electron gas the Korringa product $\mathcal{S}_0 = K_K^2 T_{1K} T = (\hbar/4\pi k_B)(\gamma_e/\gamma_n)^2$ is a constant; here K_K is the conduction-band Knight shift and γ_e and γ_n are the electron and nuclear gyromagnetic ratios, respectively. For $\gamma_n = \gamma(^{19}\text{F})$ $\mathcal{S}_0 = 2.973\times10^{-7}$ s K, which for $T_{1K}T \gtrsim 300$ s K yields a free-electron estimate of a upper bound $|K_K| < 32(2)$ ppm on the Knight shift. This lies between the negative intercept $K_0 = -7$ ppm of the Clogston-Jaccarino plot (Fig. 10) and the observed full shift $K(T\to\infty) - K(T{=}0)$ of roughly 70 ppm (Fig. 4) and is therefore consistent with the data, although the diamagnetic contribution is unknown (Sec. IV B 1). A value of $\mathcal{S}$ for LOFBS much larger than $\mathcal{S}_0$ seems unlikely; in nontransition elemental metals, e.g., $K^2 T_{1K} T/\mathcal{S} \lesssim 2$ [49].

This result can be used to obtain an estimated upper limit on the ^{19}F/conduction-band hyperfine field, given by

$$H_{\rm hf} = K_K/\mu_B N(E_F) \tag{11}$$

in the free-electron approximation [49]. With the upper bound on $|K_K|$ and the band-theoretic density of states $N(E_F) = 1.31\ \text{eV}^{-1}$/formula unit [53,54], $H_{\rm hf} < 4.2\ \text{kOe}/\mu_B$ from Eq. (11). Lattice sums yield dipolar fields from Bi moments at F sites that are an order of magnitude smaller than this. For comparison, $N(E_F) = 0.47\ \text{eV}^{-1}$/formula unit [53,54] and $H_{\rm hf} < 180\ \text{kOe}/\mu_B$ for Gd^{3+} impurities in the 3D metal $La_{1-c}Gd_cAl_2$ [32,58].

2. Coupling mechanisms: LD, TD, BGS

McHenry, Silbernagel, and Wernick [32] (MSW) reviewed potential mechanisms for host nuclear relaxation by paramagnetic impurities in metals. Their data for the $La_{1-c}Gd_cAl_2$ system fit the root-exponential relaxation function $\exp[-(t/\tau_1)^{1/2}]$ expected from dipolar relaxation in the dilute limit [33]. Stretched-exponential relaxation $\exp[-(t/\tau_1)^p]$ is observed in LOFBS, albeit with a larger power $p \approx 0.7$–0.8 (Sec. III C). Relations appropriate for $p = \frac{1}{2}$ are used in the following, with the understanding that the results are only qualitative.

Mechanisms for host nuclear relaxation by paramagnetic defects[3] [32,59] include coupling via dipolar fields to longitudinal and transverse defect-spin fluctuations (LD and TD, respectively), RKKY coupling [Benoit–de Gennes–Silhouette (BGS) [60]], and coupling to virtual defect-spin excitations [Giovannini-Heeger (GH) [61]]. For the LD, TD, and BGS mechanisms the root-exponential rate $1/\tau_1$ at high temperatures is related to the defect-spin correlation time τ_c by [32]

$$\frac{1}{\tau_1(\tau_c)} = |\Gamma|^2 \frac{\tau_c}{1+(\omega_i\tau_c)^2}. \tag{12}$$

Here $|\Gamma|^2$ is the nuclear-spin–defect-spin coupling coefficient and $\omega_i = \gamma_i H_0$, with $i = n$ (nuclear) for the LD mechanism and $i = m$ (magnetic defect) for the TD and BGS mechanisms. The observed ^{19}F spin-lattice relaxation field and temperature dependencies in LOFBS (Fig. 8) strongly suggest this behavior, with τ_c a monotonically decreasing function of increasing temperature. The GH mechanism yields a temperature- and field-independent rate apart from the saturation effect discussed in Appendix C, and is not considered further.

From Eq. (12) $1/\tau_1(\tau_c)$ exhibits a maximum $1/\tau_{1\,\rm max}$ for $\omega_i\tau_c = 1$, so that $|\Gamma|^2 = 2\omega_i/\tau_{1\,\rm max}$. These differ for TD/BGS and LD by the large factor ω_m/ω_n.

Calculated values of $|\Gamma|^2_{\rm calc}$ at high temperatures for the three mechanisms in the free-electron approximation are [32]

$$\text{LD: } |\Gamma|^2_{\rm calc} = 16\pi^3(\gamma_n M_{\rm sat})^2 \tfrac{1}{3}(J+1)/J \times \overline{\sin^2\theta\,\cos^2\theta}, \tag{13}$$

[3]The term "defect" is used instead of the more usual "impurity" to include the hypothetical Bi $6p$ magnetic defects discussed in Sec. IV A 2.

TABLE III. Experimental and calculated spin-lattice relaxation coupling coefficients in LOFBS, $H_0 = 11.74$ kOe. *Observed*: maximum rate $1/\tau_{1\,\max} = 5.23(5)\ \mathrm{s}^{-1}$ (Fig. 8), temperature of maximum $T_{\max} = 8.316$ K. *Calculated*: correlation time $\tau_c(T_{\max}) = 1/\omega_i$, coupling constant $|\Gamma|^2_{\rm expt} = 2\omega_i/\tau_{1\,\max}$, $|\Gamma|^2_{\rm calc}$ (Sec. IV C 2), maximum static exponential relaxation rate $T_{2e}^{*-1}(\max) = 7.2(6)\times10^4\ \mathrm{s}^{-1}$.

Mechanism	ω_i (s^{-1})	$\tau_c(T_{\max})$ (s)	$\lvert\Gamma\rvert^2_{\rm expt}$ (s^{-2})	$\lvert\Gamma\rvert_{\rm expt}$ (s^{-1})	$\lvert\Gamma\rvert_{\rm calc}$ (s^{-1})	$\lvert\Gamma\rvert_{\rm calc}/\lvert\Gamma\rvert_{\rm expt}$	$\lvert\Gamma\rvert_{\rm expt}/T_{2e}^{*-1}(\max)$
LD ($\omega_i = \omega_n$)	2.96×10^8	3.38×10^{-9}	$3.09(3)\times10^9$	$5.56(3)\times10^4$	6.21×10^4[a]	1.117(6)	0.77(7)
TD ($\omega_i = \omega_m$)	2.55×10^{11}	3.93×10^{-12}	$2.66(3)\times10^{12}$	$1.631(8)\times10^6$	9.49×10^4[b]	0.06	23
BGS ($\omega_i = \omega_m$)	”	”	”	”	<32.9[c]	$<2\times10^{-5}$	”

[a]From Eq. (13).
[b]From Eq. (14).
[c]Upper limit from Eq. (15)using $N(E_F)\mathcal{J}_{\rm ex}$ from Eq. (16).

$$\text{TD: } |\Gamma|^2_{\rm calc} = \frac{8\pi^3}{9}(\gamma_n M_{\rm sat})^2 \tfrac{1}{3}(J+1)/J \times \overline{[(1-3\cos^2\theta)^2 + 9\sin^4\theta]}, \quad (14)$$

$$\text{BGS: } |\Gamma|^2_{\rm calc} = \frac{16\pi^3}{9}\left(\frac{\pi A \mathcal{J}_{\rm ex} N^2(E_F) E_F N_0 c}{2\hbar k_F^3}\right)^2 \frac{1}{3}J(J+1), \quad (15)$$

where $M_{\rm sat} = N_0 c\,\mu_{\rm eff}$, and the overlines are averages over angles θ to defect sites. Experimental and calculated values of $|\Gamma|^2$ for these mechanisms are given in Table III. Their comparison yields strong evidence that the LD mechanism is dominant in LOFBS.

There is reasonable agreement between calculated and experimental values for the LD results ($|\Gamma|^2_{\rm calc}/|\Gamma|^2_{\rm exp} \approx 1$), but there is a large discrepancy for the TD results: $|\Gamma|^2_{\rm calc}/|\Gamma|^2_{\rm exp} \ll 1$. In addition, the ratio $|\Gamma|_{\rm exp}/T_{2e}^{*-1}(\max)$, where $T_{2e}^{*-1}(\max) = A_{T_{2e}^*} M_{\rm sat}$ is the maximum exponential static relaxation rate (Sec. IV B 2), is also of order unity for the LD mechanism; this would be expected because the two couplings were of the same origin. For the TD mechanism this ratio is $\gg 1$, which is again evidence against it.

The parameters in Eq. (15) for the BGS mechanism are defined above in Sec. IV B 2. From the upper bound on $H_{\rm hf}$ derived above in Sec. IV C 1, $A < 5.6\times10^7\ \mathrm{s}^{-1}$. Then Eq. (15) yields an upper limit for the BGS $|\Gamma|^2_{\rm calc}$ that is very much smaller than the experimental value (Table III) and can be neglected.

Equation (12) does not include the effect of saturation of defect moments at low temperatures and high fields, which leads to a reduction of $1/\tau_1$ [32]. This is treated in Appendix C, and results in a corrected rate $1/\tau_1^0(H,T)$ and coupling constant $\Gamma_0(H,T)$.

3. Defect-spin relaxation and exchange coupling

Field and temperature dependencies of τ_c. These have been determined by solving Eq. (C2) for $\tau_c(H,T)$ point by point from $\tau_1^0(H,T)$ [Fig. 15(b)] with $|\Gamma_0|^2$ from Eq. (C3). The results are shown in Fig. 12(a). The curves are solutions of Eq. (C2), not fits; the equation is quadratic in τ_c and its two solutions are on opposite sides of the maximum in $1/\tau_1^0(T)$.

The results for $\tau_c(H,T)$ obtained in this way are shown in Fig. 12(b). For $H_0 = 11.74$ kOe, the data below ~100 K are roughly consistent with $\tau_c T = 2.58(7)\times10^{-8}$ s K. For $H_0 = 20$ and 40 kOe $\tau_c(T)$ is smaller than for 11.74 kOe but with essentially the same slope. This is after correction for the saturation reduction [Fig. 15(b) of Appendix C], and thus is an intrinsic field dependence. It is not well understood.

This result justifies using the Korringa expression [62,63]

$$1/\tau_c T = 4\pi(k_B/\hbar)[N(E_F)\mathcal{J}_{\rm ex}]^2, \quad (16)$$

where $\mathcal{J}_{\rm ex}$ is the defect and conduction-electron exchange coupling. Table IV gives $N(E_F)\mathcal{J}_{\rm ex}$ using the observed value of $\tau_c T$ and Eq. (16), and $\mathcal{J}_{\rm ex}$ using the average $N(E_F) = 1.31\ \mathrm{eV}^{-1}$/formula unit from band theory [53,54]. For comparison, $N(E_F)\mathcal{J}_{\rm ex}$ and $\mathcal{J}_{\rm ex}$ for dilute Gd impurities in the 3D compound $La_{1-c}Gd_cAl_2$ [32] are also given.

These results can be used to estimate the effect of the defect spins on the superconductivity of LOFBS. From the Abrikosov-Gor'kov theory [64,65], the suppression ΔT_c of T_c

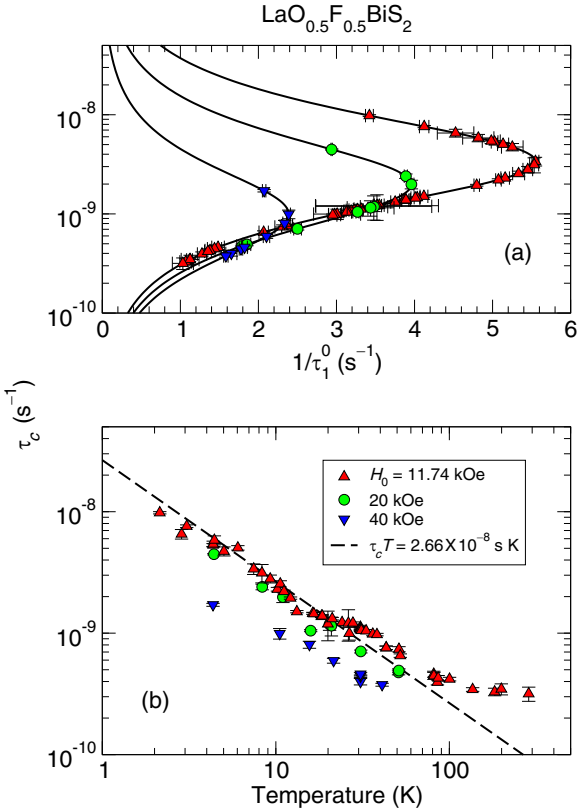


FIG. 12. (a) Defect-spin correlation times τ_c obtained from $1/\tau_1^0$ and Eq. (C1). Curves: Eq. (C2). (b) Field and temperature dependencies of τ_c. Dashed line: fit of $\tau_c T = $ const to 11.74 kOe data.

TABLE IV. Defect and conduction-band DOS spin-exchange product $N(E_F)\mathcal{J}_{ex}$ from Eq. (16), exchange constant $\mathcal{J}_{ex}$ using $N(E_F)$ from Refs. [53,54], and defect RKKY correlation times τ_m^{RKKY} from Eq. (19) for LOFBS. Values for Gd-doped $LaAl_2$ (Ref. [32]) are included for comparison.

	$N(E_F)\mathcal{J}_{ex}$	$\mathcal{J}_{ex}$ (meV)	τ_m^{RKKY} (s)
LOFBS	0.0047	3.6	2.3×10^{-7}
$La_{1-c}Gd_cAl_2$	0.09	90	6.4×10^{-10}

by a concentration c of spin-S impurities is given by

$$k_B \Delta T_c = -\frac{\pi^2}{8} c N(E_F) \mathcal{J}_{ex}^2, \tag{17}$$

which from the above results yields $\Delta T_c \approx -0.18$ mK. The effect is negligible.

Defect-defect interactions. Coupling between dilute defect spins will also affect their fluctuation spectra. For example, RKKY Gd-Gd interactions are observed to dominate Gd^{3+} spin fluctuations in $La_{1-c}Gd_cAl_2$ [32].

A rough estimate of the defect-spin fluctuation rate due to dipolar coupling is given by

$$1/\tau_m^{dip} \approx \gamma_m \mu_{eff}/R^3, \tag{18}$$

where we take $\gamma_m = \mu_{eff}/\hbar J$ using the average $\mu_{eff} \approx 3.7\mu_B$ of the two model values (Table II) for the defect moment, and $R = (3/4\pi N_0 c)^{1/3}$ is the mean spacing between local moments. This yields $\tau_c^{dip} \approx 6\times10^{-7}$ s, considerably longer than the observed values [Fig. 12(b)].

In a free-electron picture the defect RKKY correlation time τ_m^{RKKY} is given by [32]

$$1/\tau_m^{RKKY} = \tfrac{1}{9}\left[\tfrac{1}{6}\pi S(S+1)\right]^{1/2} N(E_F)\mathcal{J}_{ex}^2 c/\hbar. \tag{19}$$

Values of τ_m^{RKKY} for LOFBS and $La_{1-c}Gd_cAl_2$ from Eq. (19) are also given in Table IV. For LOFBS τ_m^{RKKY} is again considerably longer than observed. We conclude that defect-defect interactions are not important for defect-spin relaxation, so that defect-spin fluctuations are due to Korringa relaxation by conduction electrons.

These results also determine the order of magnitudes $1/\gamma_m^i\tau_m$, i = dip and RKKY, of defect spin-spin interaction fields. They are both a gauss or less, compared to the nearly 10 kOe needed for molecular-field fits to the magnetization data (Sec. IV A 2 c and Appendix B).

V. SUMMARY AND CONCLUSIONS

We have carried out a magnetization and ^{19}F NMR study of the normal-state ambient-pressure-grown $LaO_{0.5}F_{0.5}BiS_2$ (LOFBS). The measurements reveal dilute local magnetic moments of a few μ_B, the concentration of which ($\sim$1000 ppm) is an order of magnitude greater than the measured levels of $4f$ impurities. The local moments are associated with structural defects, most likely magnetic Bi $6p$ states in the BiS_2 layers that are decoupled from the conduction band by defects.

Either of two models describe the defect-moment magnetism in LOFBS: a Brillouin function model (BFM), appropriate for weakly interacting spins in a paramagnet, or a two-level scenario (TLM), in which Bi $6p$ states acquire effective moments determined by a combination of crystal electric fields and spin-orbit coupling. The TLM fits cannot determine these separately, only their ratio. Both models fit the data, but both require a Curie-Weiss argument $x = \mu_{eff}H_0/k_B(T + T_W)$. The value of the Weiss temperature T_W is close to 1.7 K for both models, but both fits deviate from the data for large x where this form is not justified. A molecular-field approximation $x = \mu_{eff}(H_0 + \Lambda M_\mu/k_BT)$ also provides good fits, but with a molecular-field constant Λ far too large to be compatible with limits on defect spin-spin interactions from the ^{19}F NMR data.

The NMR frequency shift, linewidth, and spin-lattice relaxation are consistent with a predominantly dipolar coupling between ^{19}F nuclei and defect moments. Any direct conduction-band Korringa contribution to the observed ^{19}F spin-lattice relaxation is very small, so that it is therefore dominated by defect-moment fluctuations. The defect-moment fluctuation rates $1/\tau_c$ derived from ^{19}F relaxation data exhibit Korringa relaxation τ_cT = const due to the conduction band. This is inconsistent with a picture in which the defect moments are substitutional at La sites in the blocking layers (cf. Fig. 1) as would be the case for, e.g., extrinsic $4f$ ions. The Korringa law for the defect-spin relaxation rate involves the conduction band, and we tend to favor the TLM as a more appropriate picture of $6p$ moments in defects.

The situation in LOFBS may be similar to the paramagnetism that has been detected in other bismuth compounds, particularly α-Bi_2O_3, where paramagnetism was observed at a similar concentration level [28].

There is a small anomaly in $M_{obs}(T)$ at $\sim$60 K [Fig. 2(a)], the origin of which is not clear. We note that below roughly this temperature the NMR frequency shift becomes measurable (Fig. 4), the spin-lattice relaxation rate becomes field dependent [Fig. 8(a)], and the value of the exponent on the power exponential of the relaxation rate drops [Fig. 8(b)]. It is also where the Korringa law becomes valid and τ_c shows an intrinsic field dependence (Fig 14); the latter is hard to understand. We could have speculated that these are all consistent with the TLM if Bi $6p$ electrons become trapped in defects below that temperature, but this would require knowledge of the CEF level scheme.

More experiments are needed. Magnetization and NMR studies of pressure-grown and as-grown samples and studies of samples under pressure would be useful to determine the behavior of defect spin dynamics with changes of superconducting coherence and the attainment of higher T_c's in this family of materials.

ACKNOWLEDGMENTS

This work was supported in part by grants from the National Science Foundation, Grants No. EES/CREST-2112554 and No. DMR/PREM-1523588, the University of California, Riverside Academic Senate, and the National Natural Science Foundations of China, Grant No. 12174065. Research at the University of California, San Diego, was supported by the U.S. Department of Energy, Basic Energy Sciences, under Grant No. DE-FG02-04ER46105.

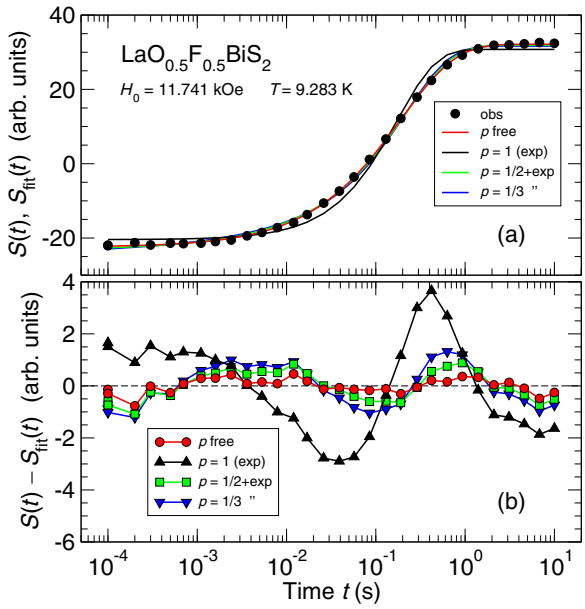


FIG. 13. (a) Recovery of ^{19}F spin-lattice relaxation signal in LOFBS powder, $H_0 = 11.74$ kOe, $T = 9.283$ K. Points: observed $S(t)$. Curves: fit functions $S_{\rm fit}(t)$ (see text). (b) Differences $S(t) - S_{\rm fit}(t)$.

APPENDIX A: STRETCHED-EXPONENTIAL FITS TO SPIN-LATTICE RELAXATION DATA

The recovery signal $S(t)$ after pulse inversion from which $s(t)$ of Fig. 7 was derived is shown in Fig. 13(a) (points), together with fits of various functions $S_{\rm fit}(t)$ to the data. These are as follows.

(1) p free: a stretched exponential $\exp[-(t/\tau_1)^p]$ with p a fit parameter,

(2) $p = 1$: a simple exponential $\exp[-(t/T_1)]$,

(3) $p = \frac{1}{2}$: the product $\exp[-(t/\tau_1)^{1/2}]\exp(-t/T_1)$ of a square-root exponential and a simple exponential, and

(4) $p = \frac{1}{3}$: the product $\exp[-(t/\tau_1)^{1/3}]\exp(-t/T_1)$ of a cube-root exponential and a simple exponential.

Figure 13(b) gives the differences $S(t) - S_{\rm fit}(t)$.

Fits to fixed-power stretched exponentials without the simple-exponential factor ($1/T_1 = 0$) are significantly worse.

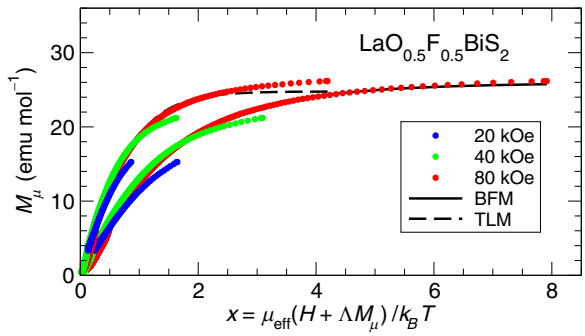


FIG. 14. Fits to the intrinsic magnetization $M_\mu(H, T)$ of the BFM (solid curve) and the TLM (dashed curve) using the molecular field *ansatz*, i.e., arguments $x = \mu_{\rm eff}(H + \Lambda M_\mu)/k_BT$ (cf. Sec. IV A 2 c).

TABLE V. Parameters from molecular-field fits of the BFM and TLM [Eqs. (2) and (3), respectively] to intrinsic magnetization $M_\mu(H, T)$ (Fig. 14).

Model	BFM	TLM
Concentration (ppm)	795(71)	1424(18)
Saturation magnetization $M_{\rm sat}$ (emu/mol)	26.1(5)	25.5(2)
Effective moment $\mu_{\rm eff}$ (μ_B)	5.8(5)	3.11(3)
J (BFM)	1.8(5)	
Spin-orbit/CEF ratio λ/Δ (TLM)		−0.56(2)
g	3.2(9)[a]	2[b]
Mol. field const. Λ (mol-Oe/emu)	−347(18)	−363(17)
Max. mol. field $\Lambda M_{\rm sat}$ (kOe)	−9.0(4)	−9.0(5)

[a] $g = \mu_{\rm eff}/J$.
[b] Fixed (cf. Ref. [55]).

A fit to the product $\exp[-(t/\tau_1)^p]\exp(-t/T_1)$ with $1/\tau_1$, p, and $1/T_1$ all free was not possible; the parameters are too strongly correlated. It can be seen from Fig. 13(b) that a stretched exponential with p a fitting parameter gives the best fit.

APPENDIX B: MOLECULAR-FIELD BFM AND TLM FITS TO THE MAGNETIZATION

Figure 14 shows the results of fits of the two models to the data assuming a molecular field, i.e., for the argument $x = \mu_{\rm eff}(H_0 + \Lambda M_\mu)/k_BT$. Table V gives the best-fit parameters. Compared with the Curie-Weiss BFM and TLM fit values (Table II), the parameters $M_{\rm sat}$, $\mu_{\rm eff}$, BFM J, TLM λ/Δ, and g differ by no more than a factor of 2. The unphysically large values of the molecular field constant Λ are discussed in Sec. IV A 2 c.

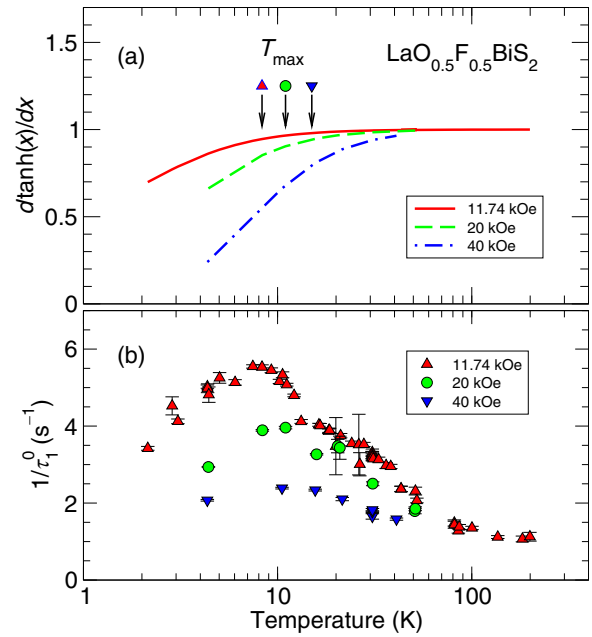


FIG. 15. Field and temperature dependencies of factors in Eq. (C1). (a) Saturation coefficient $d\ \tanh(x)/dx$. Symbols: temperatures $T_{\rm max}$ where $1/\tau_1$ is maximum. (b) Relaxation rate $1/\tau_1^0$.

APPENDIX C: SATURATION EFFECTS

Equation (12) does not include the effect of saturation of defect moments at low temperatures and high fields, which leads to a reduction of $1/\tau_1$ [32]. We assume the TLM for analysis of this effect; a BFM analysis (not shown) produces nearly the same numerical results.

For the LD mechanism the modification of Eq. (12) is of the form [32,60]

$$\frac{1}{\tau_1} = \frac{1}{\tau_1^0}\frac{d\tanh(x)}{dx}, \tag{C1}$$

so that

$$\frac{1}{\tau_1^0(T)} = |\Gamma_0(H_0,T)|^2\frac{\tau_c(T)}{1+[\omega_i\tau_c(T)]^2}, \tag{C2}$$

with

$$|\Gamma_0(H_0,T)|^2 = \frac{|\Gamma|^2}{d\tanh(x)/dx}. \tag{C3}$$

Figure 15(a) gives $d\tanh(x)/dx$ using the Curie-Weiss form $x = \mu_{\rm eff}H/k_B(T+T_W)$ with $T_W = 1.7$ K from fits to the magnetization data (Table II).

Although the reduction of $\tanh(x)/dx$ at and below $T_{\rm max}$ is significant for $H_0 = 20$ kOe and especially 40 kOe [Fig. 15(a)], for $H_0 = 11.74$ kOe $1/\tau_1^0(T_{\rm max})$ from Eq. (C1) is modified by less than 10% and the conclusions of Sec. IV C 2 above are not affected. The field and temperature dependencies of $1/\tau_1^0$ obtained from $1/\tau_1$ and Eq. (C1) are shown in Fig. 15(b).

[1] Y. Mizuguchi, H. Fujihisa, Y. Gotoh, K. Suzuki, H. Usui, K. Kuroki, S. Demura, Y. Takano, H. Izawa, and O. Miura, BiS_2-based layered superconductor $Bi_4O_4S_3$, Phys. Rev. B **86**, 220510(R) (2012).

[2] Y. Mizuguchi, S. Demura, K. Deguchi, Y. Takano, H. Fujihisa, Y. Gotoh, H. Izawa, and O. Miura, Superconductivity in novel BiS_2-based layered superconductor $LaO_{1-x}F_xBiS_2$, J. Phys. Soc. Jpn. **81**, 114725 (2012).

[3] C. T. Wolowiec, B. D. White, I. Jeon, D. Yazici, K. Huang, and M. B. Maple, Enhancement of superconductivity near the pressure-induced semiconductor-metal transition in the BiS_2-based superconductors $LnO_{0.5}F_{0.5}BiS_2$ (Ln = La, Ce, Pr, Nd), J. Phys.: Condens. Matter **25**, 422201 (2013).

[4] D. Yazici, I. Jeon, B. White, and M. Maple, Superconductivity in layered BiS_2-based compounds, Phys. C (Amsterdam) **514**, 218 (2015).

[5] R. Sogabe, Y. Goto, T. Abe, C. Moriyoshi, Y. Kuroiwa, A. Miura, K. Tadanaga, and Y. Mizuguchi, Improvement of superconducting properties by high mixing entropy at blocking layers in BiS_2-based superconductor $REO_{0.5}F_{0.5}BiS_2$, Solid State Commun. **295**, 43 (2019).

[6] Y. Mizuguchi, Material development and physical properties of BiS_2-based layered compounds, J. Phys. Soc. Jpn. **88**, 041001 (2019).

[7] C. T. Wolowiec, D. Yazici, B. D. White, K. Huang, and M. B. Maple, Pressure-induced enhancement of superconductivity and suppression of semiconducting behavior in $LnO_{0.5}F_{0.5}BiS_2$ (Ln = La,Ce) compounds, Phys. Rev. B **88**, 064503 (2013).

[8] S. Li, H. Yang, D. Fang, Z. Wang, J. Tao, X. Ding, and H. Wen, Strong coupling superconductivity and prominent superconducting fluctuations in the new superconductor $Bi_4O_4S_3$, Sci. China: Phys. Mech. Astron. **56**, 2019 (2013).

[9] X. Zhang, Q. Liu, J. Luo, A. J. Freeman, and A. Zunger, Hidden spin polarization in inversion-symmetric bulk crystals, Nat. Phys. **10**, 387 (2014).

[10] S.-L. Wu, K. Sumida, K. Miyamoto, K. Taguchi, T. Yoshikawa, A. Kimura, Y. Ueda, M. Arita, M. Nagao, S. Watauchi, I. Tanaka, and T. Okuda, Direct evidence of hidden local spin polarization in a centrosymmetric superconductor $LaO_{0.55}F_{0.45}BiS_2$, Nat. Commun. **8**, 1919 (2019).

[11] Y. A. Bychkov and E. I. Rashba, Properties of a 2D electron-gas with lifted spectral degeneracy, Pis'ma Zh. Eksp. Teor. Fiz. **39**, 66 (1983) [JETP Lett. **39**, 78 (1984)].

[12] G. Dresselhaus, Spin-orbit coupling effects in zinc blende structures, Phys. Rev. **100**, 580 (1955).

[13] Y. Mizuguchi, Review of superconductivity in BiS_2-based layered materials, J. Phys. Chem. Solids **84**, 34 (2015), focus issue on the study of matter at extreme conditions and related phenomena.

[14] Y. Mizuguchi, Discovery of BiS_2-based superconductor and material design concept, Condens. Matter **2**, 6 (2017).

[15] Y. Kopelevich, P. Esquinazi, J. H. S. Torres, and S. Moehlecke, Ferromagnetic- and superconducting-like behavior of graphite, J. Low Temp. Phys. **119**, 691 (2000).

[16] P. Esquinazi, D. Spemann, R. Höhne, A. Setzer, K. H. Han, and T. Butz, Induced magnetic ordering by proton irradiation in graphite, Phys. Rev. Lett. **91**, 227201 (2003).

[17] O. V. Yazyev and L. Helm, Defect-induced magnetism in graphene, Phys. Rev. B **75**, 125408 (2007).

[18] J. Červenka, M. I. Katsnelson, and C. F. J. Flipse, Room-temperature ferromagnetism in graphite driven by two-dimensional networks of point defects, Nat. Phys. **5**, 840 (2009).

[19] M. Sepioni, R. R. Nair, S. Rablen, J. Narayanan, F. Tuna, R. Winpenny, A. K. Geim, and I. V. Grigorieva, Limits on intrinsic magnetism in graphene, Phys. Rev. Lett. **105**, 207205 (2010).

[20] Y. G. Semenov, J. M. Zavada, and K. W. Kim, Weak ferromagnetism of antiferromagnetic domains in graphene with defects, Phys. Rev. B **84**, 165435 (2011).

[21] P. Dev, Y. Xue, and P. H. Zhang, Defect-induced intrinsic magnetism in wide-gap III nitrides, Phys. Rev. Lett. **100**, 117204 (2008).

[22] M. Venkatesan, C. B. Fitzgerald, and J. M. D. Coey, Unexpected magnetism in a dielectric oxide, Nature (London) **430**, 630 (2004).

[23] C. Das Pemmaraju and S. Sanvito, Ferromagnetism driven by intrinsic point defects in HfO_2, Phys. Rev. Lett. **94**, 217205 (2005).

[24] H. Pan, J. B. Yi, L. Shen, R. Q. Wu, J. H. Yang, J. Y. Lin, Y. P. Feng, J. Ding, L. H. Van, and J. H. Yin, Room-temperature fer-

romagnetism in carbon-doped ZnO, Phys. Rev. Lett. **99**, 127201 (2007).
[25] P. D. Esquinazi, W. Hergert, M. Stiller, L. Botsch, H. Ohldag, D. Spemann, M. Hoffmann, W. A. Adeagbo, A. Chassé, S. K. Nayak, and H. Ben Hamed, Defect-induced magnetism in non-magnetic oxides: Basic principles, experimental evidence, and possible devices with ZnO and TiO_2, Phys. Status Solidi B **257**, 1900623 (2020).
[26] N. E. Ainbinder, G. A. Volgina, E. A. Kravchenko, A. N. Osipenko, A. A. Gippius, S. H. Fam, and A. Bush, ^{209}Bi NQR powder spectra influenced by local and applied magnetic fields, Z. Naturforsch. A **49**, 425 (1994).
[27] A. Kharkovskii, V. Nizhankovskii, E. A. Kravchenko, and V. G. Orlov, Magnetic properties of the bismuth oxide $\alpha - Bi_2O_3$, Z. Naturforsch. A **51**, 665 (1996).
[28] E. A. Kravchenko, V. G. Orlov, and M. P. Shlykov, Magnetic properties of bismuth(III) oxy compounds, Russ. Chem. Rev. **75**, 77 (2006).
[29] P. Esquinazi, W. Hergert, D. Spemann, A. Setzer, and A. Ernst, Defect-induced magnetism in solids, IEEE Trans. Magn. **49**, 4668 (2013).
[30] C. P. Slichter, *Principles of Magnetic Resonance*, 3rd ed., Springer Series in Solid-State Sciences (Springer, New York, 1996).
[31] R. E. Walstedt and L. R. Walker, Nuclear-resonance line shapes due to magnetic impurities in metals, Phys. Rev. B **9**, 4857 (1974).
[32] M. R. McHenry, B. G. Silbernagel, and J. H. Wernick, Impurity-induced nuclear spin-lattice relaxation in metals: A new approach, Phys. Rev. Lett. **27**, 426 (1971); Nuclear spin-lattice relaxation in the $La_{1-c}Gd_cAl_2$ intermetallic compounds, Phys. Rev. B **5**, 2958 (1972).
[33] D. Tse and S. R. Hartmann, Nuclear spin-lattice relaxation via paramagnetic centers without spin diffusion, Phys. Rev. Lett. **21**, 511 (1968).
[34] D. C. Johnston, Stretched exponential relaxation arising from a continuous sum of exponential decays, Phys. Rev. B **74**, 184430 (2006).
[35] A. Athauda and D. Louca, Nanoscale atomic distortions in the BiS_2 superconductors: Ferrodistortive sulfur modes, J. Phys. Soc. Jpn. **88**, 041004 (2019).
[36] D. Yazici, K. Huang, B. D. White, A. H. Chang, A. J. Friedman, and M. B. Maple, Superconductivity of F-substituted $LnOBiS_2$ (Ln=La, Ce, Pr, Nd, Yb) compounds, Philos. Mag. **93**, 673 (2013).
[37] J. Zhang, K. Huang, Z. F. Ding, D. E. MacLaughlin, O. O. Bernal, P.-C. Ho, C. Tan, X. Liu, D. Yazici, M. B. Maple, and L. Shu, Superconducting gap structure in ambient-pressure-grown $LaO_{0.5}F_{0.5}BiS_2$, Phys. Rev. B **94**, 224502 (2016).
[38] Y. Fang, C. T. Wolowiec, A. J. Breindel, D. Yazici, P. C. Ho, and M. B. Maple, Upper critical magnetic field of $LnO_{0.5}F_{0.5}BiS_2$ (Ln = La, Nd) superconductors at ambient and high pressure, Supercond. Sci. Technol. **30**, 115004 (2017).
[39] C. R. Bruce, F^{19} nuclear magnetic resonance line shapes in CaF_2, Phys. Rev. **107**, 43 (1957).
[40] I. J. Lowe and R. E. Norberg, Free-induction decays in solids, Phys. Rev. **107**, 46 (1957).
[41] D. E. Barnaal and I. J. Lowe, Measured nuclear magnetic resonance free-induction-decay shapes and moments for F^{19} in CaF_2, Phys. Rev. **148**, 328 (1966).
[42] N. W. Ashcroft and N. D. Mermin, *Solid State Physics* (Harcourt College Publishers, Boston, 1976).
[43] M. R. Crook and R. Cywinski, Voigtian Kubo-Toyabe muon spin relaxation, J. Phys.: Condens. Matter **9**, 1149 (1997).
[44] A. Sadoc, M. Body, C. Legein, M. Biswal, F. Fayon, X. Rocquefelte, and F. Boucher, NMR parameters in alkali, alkaline earth and rare earth uorides from first principle calculations, Phys. Chem. Chem. Phys. **13**, 18539 (2011).
[45] A. M. Clogston, A. C. Gossard, V. Jaccarino, and Y. Yafet, Orbital paramagnetism and the knight shift in transition metal superconductors, Rev. Mod. Phys. **36**, 170 (1964).
[46] A. Abragam, *The Principles of Nuclear Magnetism* (Oxford University Press, Oxford, 1961).
[47] W. E. Blumberg, Nuclear spin-lattice relaxation caused by paramagnetic impurities, Phys. Rev. **119**, 79 (1960).
[48] L. B. Mendelsohn, F. Biggs, and J. B. Mann, Hartree-Fock diamagnetic susceptibilities, Phys. Rev. A **2**, 1130 (1970).
[49] G. C. Carter, L. H. Bennett, and D. J. Kahan, *Metallic Shifts in NMR*, in Progress in Materials Science, Vol. 20 (Pergamon, Oxford, 1977), Chap. 2.
[50] J. Shao, Z. Liu, X. Yao, L. Zhang, L. Pi, S. Tan, C. Zhang, and Y. Zhang, Superconducting properties of $BiSe_2$-based $LaO_{1-x}F_xBiSe_2$ single crystals, Europhys. Lett. **107**, 37006 (2014).
[51] N. Kase, Y. Terui, T. Nakano, and N. Takeda, Superconducting gap symmetry of the BiS_2-based superconductor $LaO_{0.5}F_{0.5}BiSSe$ elucidated through specific heat measurements, Phys. Rev. B **96**, 214506 (2017).
[52] E. G. Batyev, Pauli paramagnetism and Landau diamagnetism, Phys. Usp. **52**, 1245 (2009).
[53] I. R. Shein and A. L. Ivanovskii, Electronic band structure and Fermi surface for new layered superconductor $LaO_{0.5}F_{0.5}BiS_2$ in comparison with parent phase $LaOBiS_2$ from first principles, JETP Lett. **96**, 769 (2013).
[54] B. Li, Z. W. Xing, and G. Q. Huang, Phonon spectra and superconductivity of the BiS_2-based compounds $LaO_{1-x}F_xBiS_2$, Europhys. Lett. **101**, 47002 (2013).
[55] C. Kittel, *Introduction to Solid State Physics*, 8th ed. (Wiley, Hoboken, NJ, 2005), Chap. 11, p. 311.
[56] J.-W. Luo, G. Bester, and A. Zunger, Full-zone spin splitting for electrons and holes in bulk GaAs and GaSb, Phys. Rev. Lett. **102**, 056405 (2009).
[57] P. Boutron, Exact calculation of the paramagnetic susceptibility of a single crystal with arbitrary crystal field and exchange interactions, Phys. Rev. B **7**, 3226 (1973).
[58] B. G. Silbernagel and J. H. Wernick, Nuclear magnetic resonance in $LaAl_2$, Phys. Rev. B **7**, 4787 (1973).
[59] B. Giovannini, P. Pincus, G. Gladstone, and A. J. Heeger, Nuclear relaxation in dilute magnetic alloys, J. Phys. Colloq. **32**, C1-163 (1971).
[60] H. Benoit, P.-G. de Gennes, and D. Silhouette, Relaxation nucléaire dans certains alliages de terres rares paramagnétiques [Nuclear Relaxation in certain alloys of paramagnetic rare earths], Compt. Rend. **256**, 3841 (1963).
[61] B. Giovannini and A. Heeger, Relaxation des spins nucléaires dans les alliages dilués, Solid State Commun. **7**, 287 (1969).
[62] R. Taylor, Electron spin resonance of magnetic ions in metals an experimental review, Adv. Phys. **24**, 681 (1975).

[63] S. Barnes, Theory of electron spin resonance of magnetic ions in metals, Adv. Phys. **30**, 801 (1981).

[64] A. A. Abrikosov and L. P. Gor'kov, Contribution to the theory of superconducting alloys with paramagnetic impurities, Zh. Eksp. Teor. Fiz. **39**, 1781 (1960) [Sov. Phys. JETP **12**, 1243 (1961)].

[65] E. Müller-Hartmann and J. Zittartz, Theory of magnetic impurities in superconductors. II, Z. Phys. **234**, 58 (1970).